

Thermomechanical Phase Change Peridynamic Model for Welding Analysis

Bingquan Wang, Selda Oterkus* and Erkan Oterkus

Peridynamics Research Centre, Department of Naval Architecture, Ocean and Marine Engineering, University of Strathclyde, Glasgow G4 0LZ United Kingdom

Abstract

In numerical welding modelling, it is critically important to adopt a heat source model that fits the actual welding process since the heat source model has significant influence on the calculation accuracy of the transient welding temperature field, especially near the heat source. An inappropriate source model can produce an overestimated or underestimated temperature field, leading to displacement field errors in the mechanical analysis. In this study, a new non-linear transient peridynamic model employing a variety of heat source models is developed to predict the temperature distribution and displacement variation. More importantly, as an essential physical phenomenon in heat conduction, phase transformation is considered in the peridynamic model. The importance of how the latent heat in the phase change can affect the temperature distribution and displacement field is also emphasized. The simulation results are compared with the finite element method results. Close agreements are observed which demonstrates the capability of the proposed non-linear transient peridynamic model for thermomechanical phase change analysis for welding modelling.

Keywords: peridynamics; thermomechanical; phase change; welding

Nomenclature

a	Thermal diffusivity
a_h, b_h, c_h	Heat source parameters
α	Thermal expansion coefficient
\mathbf{b}	Body force density
c	Bond constant
C_l	Specific heat capacity at liquidus
C_p	Specific heat capacity in the mushy zone
C_s	Specific heat capacity at solidus
C_v	Effective heat capacity
δ	Horizon size
Δx	Spacing between material points
E	Young's Modulus
f_h	Heat flow density

*Correspond author: selda.oterkus@strath.ac.uk

h	Geometrical thickness
h_q	Volumetric heat generation
H	Plate thickness
\mathbf{n}	Normal vector
N	Welding track divisions
k	Thermal conductivity
κ	Micro-thermal conductivity
L	Length
L_T	Latent heat
L_W	Welding track length
P	Point heat source power
q	Heat flux
q_m	Maximum heat density at arc centre
Q	Laser power / net heat input per unit time
ρ	Density
R	Distance to the centre of the welding arc
R_C	Fictitious region in PD
R_t	Real region in PD
s	Stretch between two material points
σ	Heat source distribution parameter
t	Current time
t_T	Total time for the welding arc moves on the welding track
θ	Temperature
θ_b	Boundary temperature
θ_f	Fictitious region temperature
θ_0/θ_i	Initial temperature
θ_l	Fusion temperature
θ_s	Solidification temperature
v	Speed of arc
V	Volume
η	Relative displacement
W	Width
ξ	Relative position before deformation
\mathbf{x}	Position of the material points
\mathbf{x}_b	Position of the material points at real region
\mathbf{x}_f	Position of the material points at fictitious region
\mathbf{x}_i	Growth of the phase boundary

1. Introduction

Welding is a well-recognized mutual fabrication process in the manufacturing industry that utilizes high temperatures to melt the parts together. The elevated welding temperature field not only determines the welding stress field but also has a close relationship with the metallurgy, crystallization, and phase transformation processes. Various heat source models have been

proposed in the past decades to investigate heat transfer mechanisms for welding and additive manufacturing processes. The welding heat source model can be classified as a concentrated heat source, a planar distribution heat source, or a volumetric distributed heat source which depends on different welding methods in the manufacturing process. While the part of the workpiece concerned is far away from the weld's centreline, the welding heat source can be treated as a centralized heat source model. Rosenthal [1] stated an analytical solution of the temperature field for a semi-infinite body subjected to a constant heat source. For general arc welding, the welding arc's heat flow is distributed in a particular area on the weldment. Hence, a plane distribution heat source can be considered in the numerical model. Eagar et al. [2] adopted Rosenthal's theory to a two-dimensional heat source model and find the analytical solution of the temperature field. However, for high-energy beam welding, due to large depth-to-width ratio of the weld, it shows that the heat flow of the welding heat source has a great influence along the thickness direction of the workpiece, and it must be treated according to a certain volumetric distributed heat source model. Goldak et al. [3] proposed a three-dimensional double ellipsoidal model to overcome the penetration effect due to the surface heat model and Nguyen et al. [4] provided the analytical solutions for the transient temperature of the three-dimensional heat source.

Moreover, due to the complexity of the heat transfer in welding and additive manufacturing process, rapid change of the temperature can induce residual stresses and macro-thermal deformations [5]. Therefore, in the investigation of welding manufacturing process, the thermomechanical coupling effects shall be considered in thermal and structural fields. Goldak et al. [6] proposed a finite element model (FEM) for welding heat sources to investigate the temperature distribution. Van Elsen et al. [7] used a finite difference model (FDM) for moving heat sources in a semi-infinite medium. Ning et al. [8] utilized an analytical model with moving point heat source in metal additive manufacturing to predict the temperature field and thermal gradient. A coupled thermo-elasticity equation has been adopted by Biot [9] to analyse the heat conduction problems.

In addition, welding heat transfer scenarios are often accompanied by phase change. It is considered as a moving boundary problem due to the undetermined moving boundary between the liquid phase and the solid phase. Due to its non-linear characteristic, only a small number of exact solutions exist. When a substance undergoes phase change like solidification, modelling of the latent heat at the solid-liquid interface is crucial in heat transfer analysis. The latent heat can be mainly handled by front tracking methods and fixed grid methods. Latif [10]

applied front tracking method which sets an additional node at the solid-liquid interface that splits a single two-phase element into two single-phase elements. This can accurately predict the location of the moving interface and precisely handle the latent heat. However, a special numerical program needs to be employed and it merely can be used for simple geometries which restricts its application in modelling the solidification process [11]. The fixed grid method treats the domain as a single continuous region where the Stefan condition is implicitly implemented in a new form of heat equations. Thus, phase boundary is described by the enthalpy, effective heat capacity or heat generation without being explicitly specified. It has the advantages of straightforward application in an existing method and the grid spacing remains fixed in the model. Consequently, no re-meshing is necessary which can be adopted in complex multi-dimensional problems. It is reported that to use the apparent heat capacity methods to handle the latent heat when a substance undergoes a phase change, the time step size shall be relatively small. As the apparent heat capacity method in the phase change interval is obtained by using the temperature integration, if the temperature in the control domain raises from the temperature below the solidus to the temperature over the liquidus in one time step, the latent heat will be neglected in the phase change [11]. Yang et al. [12] utilizes element-free Galerkin method with smoothed effective heat capacity to model a heat transfer problem.

Challenges occur due to discontinuities emerging in the heat transfer and thermoelastic problems. Such cases can relate to the phase change in the weldment [13]. Besides, nonlocality appears when steep temperature gradients exist. Peridynamics (PD), a non-local continuum mechanics formulation introduced by Silling [14] can be utilized to deal with the phenomenon of discontinuities. It has the advantage that the governing equations are in the form of integro-differential equations. There has been significant progress on peridynamics research. Diyaroglu et. al. [15] developed peridynamic wetness approach for moisture concentration analysis. Kefal et. al. [16] performed topology optimisation study of cracked structures by using peridynamics. Yang et. al. [17] developed state-based peridynamic Kirchhoff plate formulation. Vazic et. al. [18] and Candaş et. al. [19] investigated interaction of macrocrack and microcrack interactions. Ozdemir et. al. [20] and Candaş et. al. [21] performed dynamic fracture analysis of functionally graded materials by using peridynamics. De Meo et. al. [22] predicted initiation and propagation of cracks from corrosion pits. Huang et. al. [23] developed a new peridynamic model for visco-hyperelastic materials. Various peridynamic studies were also presented on thermomechanical analysis. Kilic and Madenci [24] introduced peridynamic theory for thermomechanical analysis. Oterkus et al. [25] presented the derivation of ordinary state-based

peridynamic heat conduction equation based on the Lagrangian formalism. Alpay and Madenci [26] investigated crack growth by considering fully-coupled peridynamic thermomechanical formulation. D'Antuono and Morandini [27] demonstrated thermal shock analysis by using weakly coupled peridynamics. Hu et. al. [28] used irregular nonuniform discretisation for peridynamic thermomechanical analysis. Song et. al. [29] utilised peridynamics to simulate removal of ice from frozen structures. Zhang and Qian [30] investigated damage growth in bimaterial structures by considering thermomechanical loading. Shou and Zhou [31] examined thermally induced cracking of rocks by using non-ordinary state-based peridynamics. Martowicz et. al. [32] presented phased transformation in shape memory alloys. Pathikar et. al. [33] presented thermomechanical analysis of brittle fracture. Giannakeas et. al. [34] demonstrated their simulations for thermal shock cracking in ceramics. Wang et. al. [35] studied thermally induced crack behaviour of functionally graded materials. Chen et. al. [36] showed application of full coupled peridynamic thermomechanics for concrete cracking.

In this study, a new non-linear transient peridynamic model with various heat sources will be presented for thermomechanical analysis and phase transformation to be used for welding modelling. This paper is organized as follows: Section 2 describes the peridynamic governing equations for the thermomechanical analysis along with a series of time-dependent heat sources proposed for modelling the welding numerically. The thermomechanical phase change modelling is introduced in Section 3. Section 4 illustrates the boundary conditions implemented in the numerical simulation. In Section 5, a series of classical solidification problems, i.e. Stefan's solidification and Neumann's solidification, are presented to validate the proposed peridynamic phase change model. In addition, the temperature and displacement fields predicted by point, Gaussian distribution, and volumetric distribution heat sources are numerically simulated and the effect of phase change in thermomechanical analysis is discussed. Finally, the conclusion is given in Section 6.

2. Peridynamic Thermomechanics

Peridynamics is a non-local theory and was introduced by Silling [14,37] to eliminate the problems related with discontinuities in the domain of interest. It provides an alternative expression for the continuum mechanics. The peridynamic equation is formulated in the form of an integro-differential equation instead of a partial differential equation. The concept of non-local peridynamic theory is presented in Fig. 1. The matter is discretized into a set of material points, while each material point in the domain occupies an incremental volume.

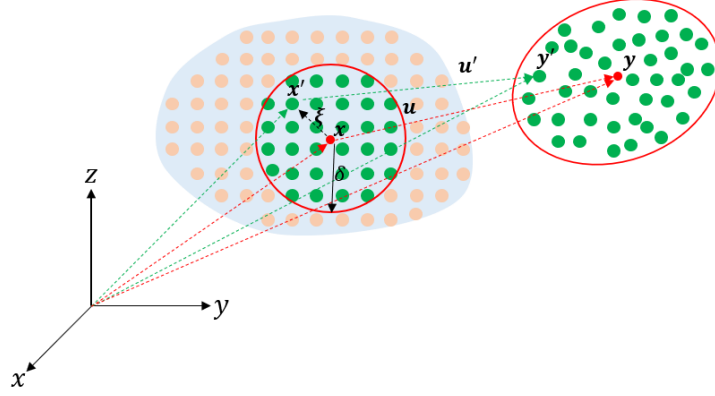


Fig. 1. Interaction of the peridynamic material point x with its family member x' .

With respect to Cartesian coordinate system, the positions of two material points x and x' prior to deformation becomes y and y' after deformation. The displacement for these material points are denoted as u and u' , respectively. The initial relative position before deformation is defined as $\xi = x' - x$ while the relative displacement is represented as $\eta = u' - u$. In addition, material points have a set family of material points and can only interact with their own family of material points. Each material point is influenced by other material points within a range, the horizon δ , which is the length scale parameter. The horizon describes the non-local behavior in peridynamic theory.

2.1. Peridynamic thermo-mechanical governing equations

The bond based thermomechanical heat transfer equation is given by [38]

$$\rho C_v \dot{\theta} = \int f_h dV' + h_q(x, t) \quad (1)$$

where ρ is the density, C_v represents the effective heat capacity, and θ is the temperature. f_h is the heat flow density [25], which can be expressed as

$$f_h = \kappa \frac{\tau}{|\xi|} \quad (2)$$

where τ is defined as

$$\tau(x, x', t) = \theta(x', t) - \theta(x, t) \quad (3)$$

and κ is the micro-thermal conductivity. For two-dimensional structures, it is provided as [25]

$$\kappa = \frac{6k}{\pi h \delta^3} \quad (4)$$

where k is the thermal conductivity and h is the thickness. For three-dimensional structures, it is defined as [25]

$$\kappa = \frac{6k}{\pi \delta^4} \quad (5)$$

The term $h_q(\mathbf{x}, t)$ in Eq.(1) represents the volumetric heat generation. In welding and additive manufacturing process, this can represent the heat raised from the heat source.

The general form of the coupled thermo-elasticity in bond-based peridynamics is provided by Oterkus et al. [38]. The equation of motion can be expressed as

$$\rho \ddot{\mathbf{u}} = \int \left[\frac{\boldsymbol{\eta} + \boldsymbol{\xi}}{|\boldsymbol{\eta} + \boldsymbol{\xi}|} c \left(s - \alpha \frac{\theta + \theta'}{2} \right) \right] dV' + \mathbf{b}(\mathbf{x}, t) \quad (6)$$

In Eq. (6) s represents the stretch between the two material points and is defined as

$$s = \frac{|\boldsymbol{\xi} + \boldsymbol{\eta}| - |\boldsymbol{\xi}|}{|\boldsymbol{\xi}|} \quad (7)$$

α is the coefficient of thermal expansion, c represents the bond constant, and \mathbf{b} is the body force density [37].

For isotropic materials, the bond constant c can be defined in terms of Young's Modulus, E and horizon size, δ [11], which can be calculated by comparing peridynamic strain energy density to the one in classical theory of elasticity. The bond constant for a two-dimensional structure can be written as [25]

$$c = \frac{9E}{\pi h \delta^3} \quad (8)$$

2.2 Description of Time Dependent Heat Sources in Welding

Heat source modelling can be classified as a point/line heat source, a planar distribution heat source, and a volumetric distributed heat source. These sources are acted on the numerical welding model depending on the actual manufacturing process model and the topographic characteristics of the weld. For typical arc welding, the heat flow of the welding arc is distributed in a certain area of the weldment, which can be utilized as a plane distribution heat source. However, for high-energy beam welding, due to the large welding seam aspect ratio,

the heat flow of the welding heat source has a great influence along the thickness direction of the workpiece and volumetric heat source should be considered.

2.2.1 Point/line heat source

In the case of welding arc/laser beam acts on the surface of thick workpieces, welding arc supplied with welding power Q can be treated as a point heat source. As shown in Fig. 2, a point heat source, so-called a concentrated source is considered for thermal analysis in the peridynamic welding model.

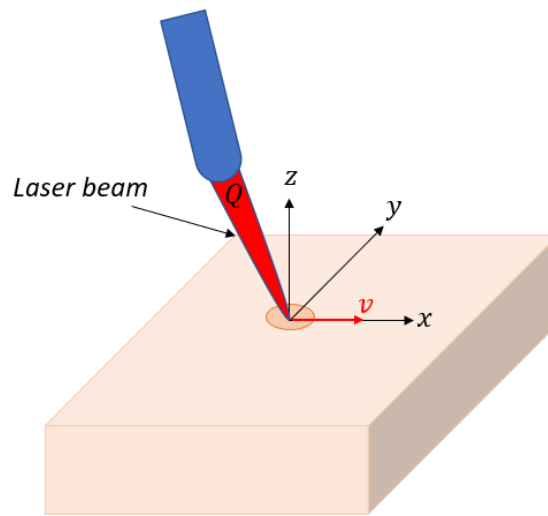


Fig. 2. Point heat source moving on the surface of a thick workpiece.

This is a simplified approximation of a physical situation but can provide a good temperature prediction under certain conditions. Rosenthal [1] provides the solution for the temperature distribution of a steady state moving point heat source acted on a semi-infinite plate as

$$\theta - \theta_0 = \frac{Q}{2\pi kR} e^{-\frac{v(x-vt+R)}{2a}} \quad (9)$$

where θ_0 is the initial temperature of the workpieces, Q is the net heat input per unit time, R is the distance to the centre of the welding arc, v is the speed of arc, t is current time and a is the thermal diffusivity.

As can be observed from Eq. (9), the temperature field in the welding arc centre tends to approach infinity when $R \rightarrow 0$, which doesn't have a physical meaning in the real welding process. However, the analytical temperature distribution for the point heat source model provides a reasonable temperature field prediction at the positions of the substance far from the heat source [39].

2.2.2 Gaussian distribution heat source

The laser beam arc is a commonly used heat source in the selective laser melting technique. The source model can be accurately represented by a Gaussian distribution heat source as [2]

$$q(x, y, t) = q_m \exp\left(-\frac{(x - v * t)^2 + y^2}{2\sigma^2}\right) \quad (10)$$

and

$$q_m = \frac{Q}{2\pi\sigma^2} \quad (11)$$

where q_m is the maximum heat density at the welding arc centre $(x - v * t, y)$, v is the speed of the moving heat source, Q is the power of laser beam, and σ is a distribution parameter. $q(x, y, t)$ represents the heat density at a point (x, y) at time t .

2.2.3 Volumetric distribution heat source

In order to consider high-energy beam welding with heat flow penetration effect in the physical manufacturing process, a volumetric distributed model, named as semi-ellipsoidal heat source model, shown in Fig. 3, has been proposed by Goldak [3].

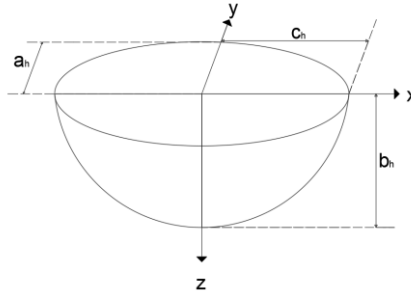


Fig. 3. Semi-ellipsoidal heat source model.

The mathematical form of heat source is given as [3]

$$q(x, y, z, t) = q_m \exp\left(-\frac{3(x - v * t)^2}{c_h^2} - \frac{3y^2}{a_h^2} - \frac{3z^2}{b_h^2}\right) \quad (12)$$

where a_h , b_h , and c_h are ellipsoidal heat source parameters as presented in Fig. 3, $x - v * t$, y , z are moving coordinates of the heat source, $q(x, y, z, t)$ is heat density at a point (x, y, z) at time t . q_m is the maximum heat density at the centre of the welding arc which is given as [3]

$$q_m = \frac{6\sqrt{Q}}{a_h b_h c_h \pi \sqrt{\pi}} \quad (13)$$

where Q is the net heat input per unit time.

3. Peridynamic Thermomechanics Coupled with Phase Change

Heat transfer scenarios with temperature variation often come with phase change. Characteristics of non-linearity due to the multi-physical nature of the processes make phase transformation challenging.

Phase change is the physical process of the matter transition state. The energy absorbed or released for a matter to transform the state is known as latent heat. Since the material can absorb or discharge a large amount of latent heat at the phase change temperature, cases such as melting and solidification of the substance subjected to the heat generated from the welding arc needs to be taken into account in the peridynamic heat conduction equation.

In the present work, the latent heat L_T is implicitly considered by effective heat capacity, in which the specific heat capacity of the material is artificially increased at mushy zone. Mushy zone is a temperature interval around the phase change temperature that the matter processes the phase transformation. The artificially increased specific heat capacity in the mushy zone can be defined as

$$C_p = \frac{L_T}{\theta_l - \theta_s} \quad (14)$$

where θ_s is the substance solidification temperature and θ_l is the substance fusion temperature. With the considered latent heat at phase change scenarios, consequently, the effective heat capacity C_v in the bond-based peridynamic heat conduction equation at different phases can be written as

$$C_v = \begin{cases} C_s & \theta < \theta_s & \text{solid phase} \\ C_p & \theta_s \leq \theta \leq \theta_l & \text{solid/liquid phase} \\ C_l & \theta > \theta_l & \text{liquid phase} \end{cases} \quad (15)$$

where C_s , C_p and C_l are specific heat capacity of the substance at solidus, mushy zone, and liquidus state, respectively. The effective heat capacity is determined by using the temperature at the material point assuming that a material point is subjected to a temperature below the melting point temperature. Therefore, the specific heat capacity at solid phase shall be used in the heat conduction equation.

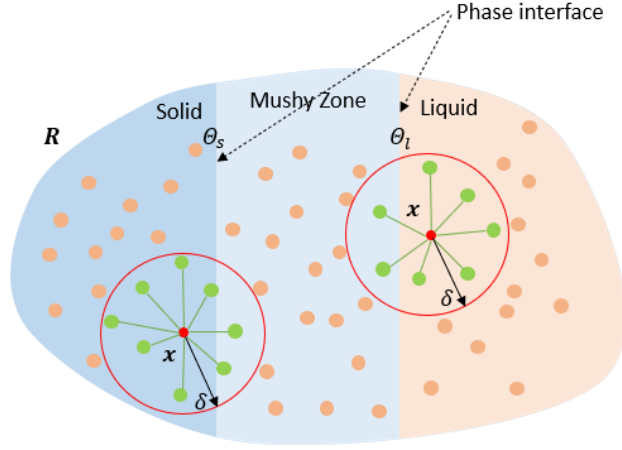


Fig. 4. Peridynamic horizon and its thermo-mechanical bonds (green line).

In addition, the mechanical characteristics of most welding or manufacturing materials are often influenced by temperature variation. More specifically, for the majority of metallic materials, the higher temperature lowers the material stiffness while in low temperature environments opposite trend is observed.

To account for the temperature influence on material stiffness behaviour in arc welding, especially for the phase change scenarios in the thermomechanical analysis, a non-local approach for modelling the temperature effect on the material stiffness is considered. In the conventional bond-based peridynamics, as shown in Fig. 1, the interaction between two material points \mathbf{x} and \mathbf{x}' is linked by a ‘bond’. The bond constant in terms of Young’s Modulus, E for a two-dimensional structure is defined by Eq. (8). Without taking into account the temperature influence in the mechanical analysis, the parameter c is a constant value.

However, in thermomechanical phase change peridynamic model for welding, the Young’s Modulus in the mechanical analysis becomes a temperature-dependent property, which can be written as $E(\theta)$. As presented in Fig. 4, a bond applied for the thermomechanical problem is described as a ‘thermo-mechanical bond’, where the temperature effect on material stiffness is considered and can be defined as

$$c(\mathbf{x}, \theta_x) = \frac{9E(\theta_x)}{\pi h \delta^3} \quad (16a)$$

and

$$c(\mathbf{x}', \theta_{x'}) = \frac{9E(\theta_{x'})}{\pi h \delta^3} \quad (16b)$$

Therefore, the temperature influence on material stiffness is represented by the bond constant. With the temperature variation on the material point and its family members, the bond constant changes correspondingly. Hence, the bond constant between two material points can be written as

$$c(\mathbf{x}, \mathbf{x}', \theta_x, \theta_{x'}) = \frac{c(\mathbf{x}, \theta_x) + c(\mathbf{x}', \theta_{x'})}{2} \quad (17)$$

With the temperature dependent bond constant, the equation of motion for coupled thermo-elasticity in bond-based peridynamics can be re-written as

$$\rho \ddot{\mathbf{u}} = \int \left[\frac{\eta + \xi}{|\eta + \xi|} c(\mathbf{x}, \mathbf{x}', \theta_x, \theta_{x'}) \left(s - \alpha \frac{\theta_x + \theta_{x'}}{2} \right) \right] dV' + \mathbf{b}(\mathbf{x}, t) \quad (18)$$

4. Application of Initial and Boundary Conditions

The initial condition of the temperature distribution can be specified at time $t = 0$

$$\theta(x, y, z, t = 0) = \theta_0(x, y, z) \quad (19)$$

where θ_0 is the initial temperature. If pre-heat treatment is adapted in the manufacturing process, θ_0 is defined as pre-heating temperature.

The boundary conditions in the heat conduction can be specified as temperature, heat flux, and the heat generation.

4.1 Temperature

The prescribed boundary temperature in peridynamics follows a distinctive technique than the loading in classical continuum mechanics. Instead of employing the prescribed temperature as a point load or distributed load, a fictitious layer R_C is introduced outside of the substance real region R_t and shown in Fig. 5 [25,40].

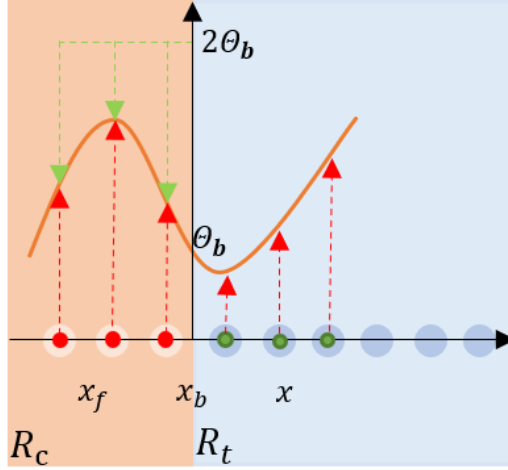


Fig. 5. Material real domain, R_t and its fictitious domain, R_c .

As represented in Fig. 5, the specified boundary temperature $\theta_b(\mathbf{x}_b, t)$ along the real material surface is implemented in the fictitious layer as [25],

$$\theta_f(\mathbf{x}_f, t + \Delta t) = 2\theta_b(\mathbf{x}_b, t + \Delta t) - \theta(\mathbf{x}, t + \Delta t) \quad (20)$$

where θ_f and θ are the temperature of material points in the fictitious region R_c and real region R_t , respectively. Note that the material points at \mathbf{x}_f and \mathbf{x} are symmetrically located with respect to the location of the boundary \mathbf{x}_b . In the case of $\theta_b(\mathbf{x}_b, t) = 0$, this represents the insulated boundary condition.

4.2 Heat flux

The implementation of the heat flux from heat source in peridynamic heat transfer equation can be achieved by evaluating the rate of the heat flow into the surface area and transforming it to the volumetric heat generation per unit volume $h_q(\mathbf{x}, t)$. Therefore, the heat flux is employed as a volumetric heat generation on the material point and can be defined as [25]

$$h_q(\mathbf{x}, t) = -\frac{q(\mathbf{x}, t) \cdot \mathbf{n}}{\Delta x} \quad (21)$$

where q is the heat flux, Δx is the spacing between material points and \mathbf{n} is the normal vector to the surface.

4.3 Time-dependent point heat source

For numerical implementation of the point source moving on the workpiece, death-live procedure for material points is introduced in this work. More specifically, the point heat source was implemented as a volumetric heat generation only, loaded on the selected material points

and the loading is moving with the time. When the heat source moves from a material point that material point will no longer generate any heat.

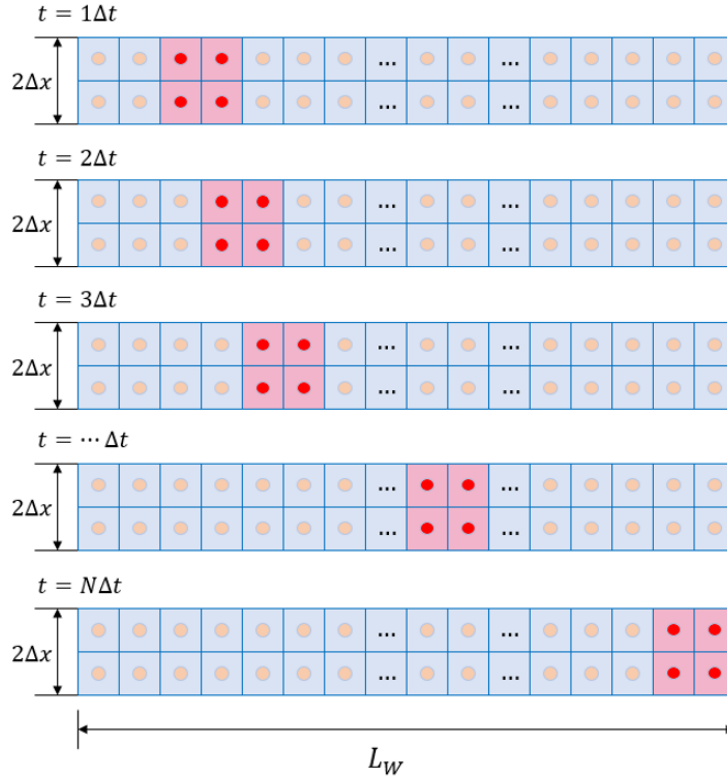


Fig. 6. Demonstration of implementing moving point heat source in the numerical model.

The principle of implementing the moving point heat source in the numerical study procedure is shown in Fig. 6. The length of the welding track is L_W and the track is discretised with N material points. The total time for the welding arc moves on the welding track is t_T . Hence the time that the heat source stays on the selected material points to generate the heat can be obtained as

$$\Delta t = \frac{t_T}{N} \quad (22)$$

5. Numerical Results

5.1 Stefan's solidification problem

Classical Stefan's solidification problem [10] is considered first. It is a moving boundary problem that describes the growth of the boundary x_i between two phases while the substance is undertaking a phase change. As presented in Fig. 7, the problem considers the substance initially stays at the fusion temperature θ_l . The surface at the one edge of the substance is suddenly maintained at temperature $\theta_b < \theta_l$ and the solidification starts instantly. The

substance is assumed only in liquid phase being active while other phase is staying at its fusion temperature.

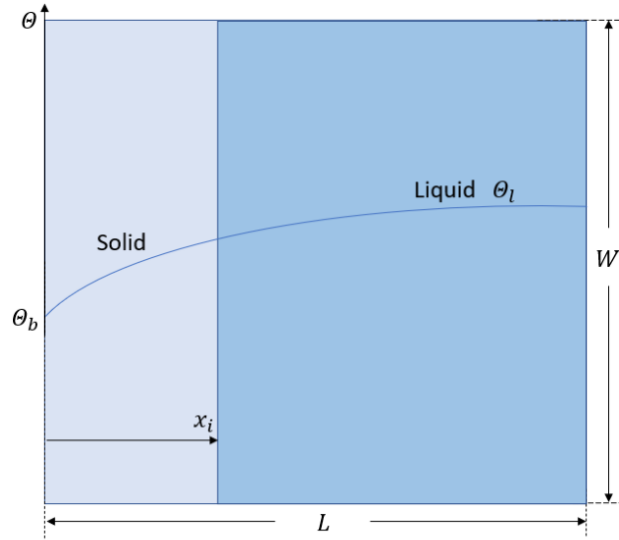


Fig. 7. Physical illustration of Stefan's solidification problem.

In this case, a solidification phenomenon of a liquid region is considered and demonstrated in Fig. 8(a) with a length of $L = 0.01\text{m}$ and width of $W = 0.01\text{m}$.

The liquid field initially stays at a constant fusion temperature, $\theta_l = 0^\circ\text{C}$. Then, it is suddenly subjected to a free surface temperature $\theta_b = -5^\circ\text{C}$ at $x = -\frac{L}{2}$. Therefore, the boundary x_i between two phases starts solidifying at $x = -\frac{L}{2}$ from $t = 0\text{s}$. Its thermal conductivity and density are specified as $k=0.6\text{W/m}^\circ\text{C}$ and $\rho=1000\text{kg/m}^3$, respectively.

In this study, the substance is assumed to undergo phase change at the phase transformation temperature range as

$$\theta_s = -1^\circ\text{C} \leq \theta \leq \theta_l = 0^\circ\text{C} \quad (23)$$

The latent heat L_T should be considered at the phase change by assuming the total latent heat required for the phase change completed is 42000J/kg . Hence, the effective heat capacity for the substance at mushy zone is

$$C_p = \frac{L_T}{\theta_l - \theta_s} = 42000\text{J/kg}^\circ\text{C} \quad (24)$$

Consequently, the specific heat capacity at different temperatures is arranged as

$$C_v = \begin{cases} C_s = 4200J/kg^{\circ}C & \theta < -1^{\circ}C \\ C_p = 42000J/kg^{\circ}C & -1^{\circ}C \leq \theta \leq 0^{\circ}C \\ C_l = 4200J/kg^{\circ}C & \theta > 0^{\circ}C \end{cases} \quad (25)$$

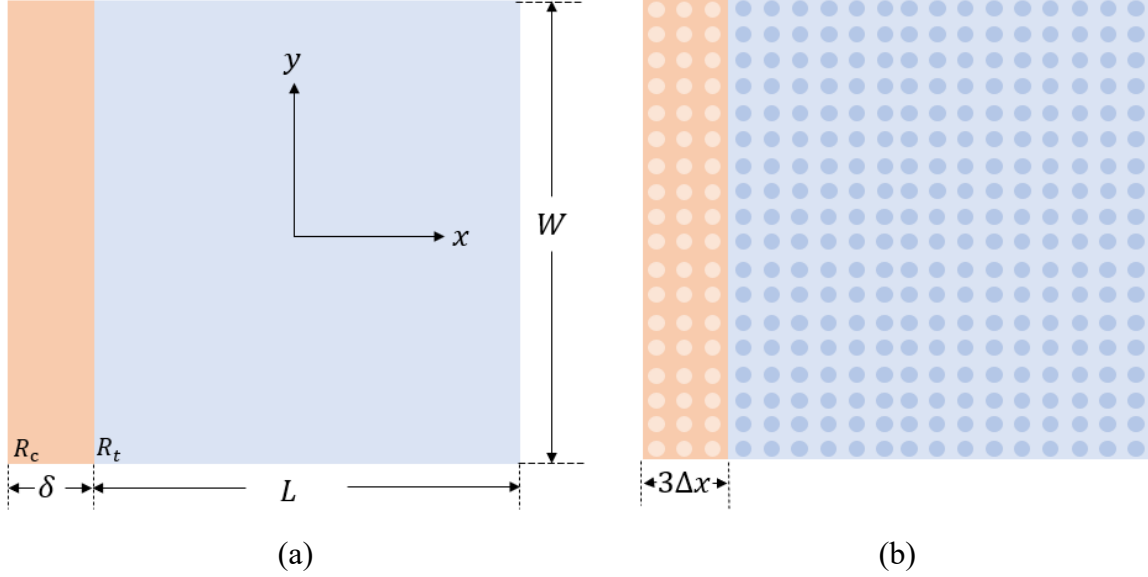


Fig. 8. Stefan's solidification problem illustration (a) geometry and (b) PD discretization. As shown in Fig. 8(b), the spacing between material points in peridynamic discretization is $\Delta x = L/100$. The horizon is chosen as $\delta = 3\Delta x$. Time step size of $\Delta t = 3 \times 10^{-2}s$ is adopted.

The initial temperature is applied as

$$\theta(x, y, t = 0) = \theta_l = 0^{\circ}C \quad (26)$$

Fictitious boundary R_c with one horizon size is added to implement the temperature boundary condition, i.e.

$$\theta\left(x = -\frac{L}{2}, y, t\right) = \theta_b = -5^{\circ}C \quad (27)$$

The temperature distribution is solved numerically by using PD and verified with the FEM in ANSYS. The temperature distribution along $(x, y = 0)$ at various time intervals ($t = 300s, t = 600s, t = 900s$) has been examined in both PD and FEM models and shown in Fig. 9. As can be observed, the PD model has a good agreement with the FEM model.

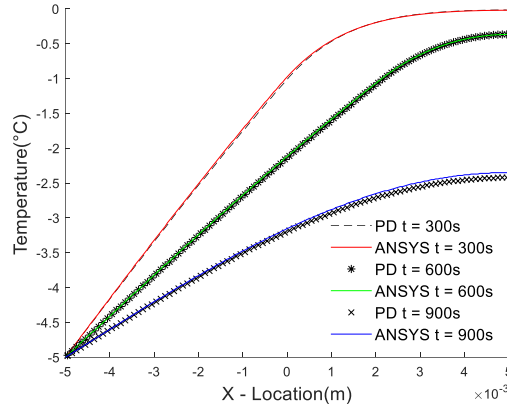


Fig. 9. Temperature comparison along axial axis at $(x, y = 0)$.

The comparison of temperature variation as a function of time at $(x = \frac{L}{2}, y = 0)$ between PD and FEM models is presented in Fig. 10. For the time between 787.82s and 797.82s, the temperature at $x = \frac{L}{2}, y = 0$ reaches $\theta_s = -1^\circ\text{C}$ which is the time that substance completely solidifies.

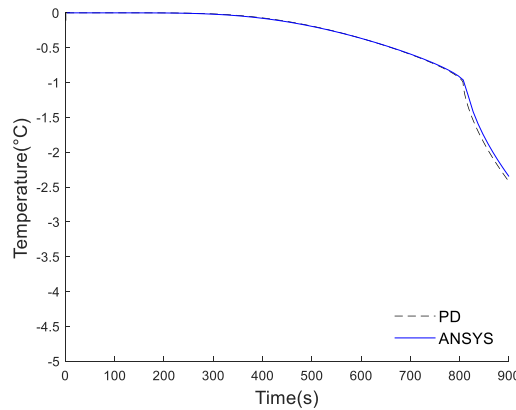


Fig. 10. Temperature variation at $(x = \frac{L}{2}, y = 0)$.

The comparison of temperature distributions for the PD and FEM models at 600s are presented in Fig. 11. As can be seen from these figures, the temperature field across the plate predicted by the PD model agrees with the FEM model.

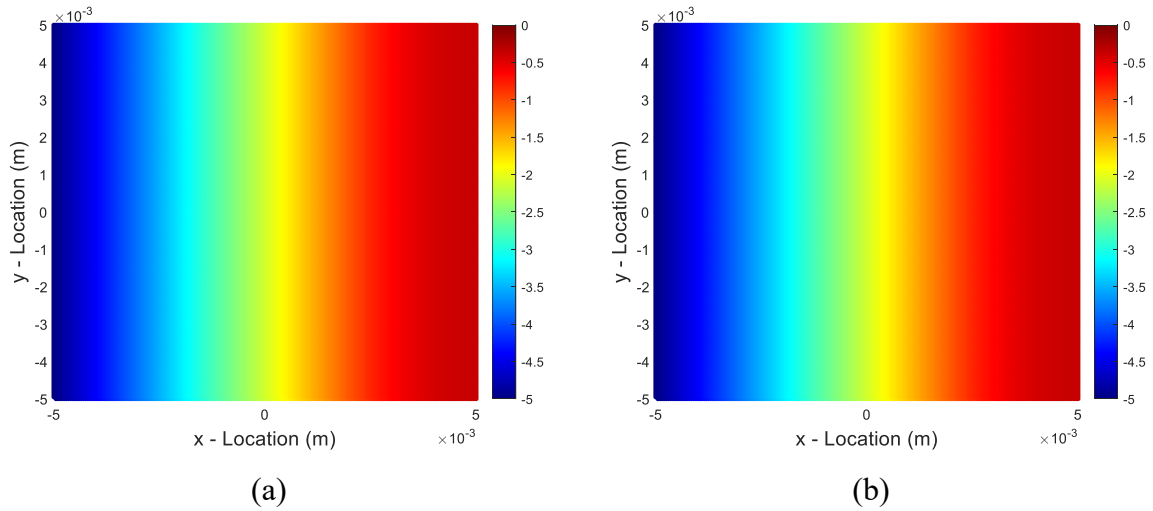


Fig. 11. Temperature distribution at $t=600s$ (a) PD (b) FEM model.

It is worth having a look at how the latent heat in the phase change can affect the temperature distribution. The Stefan's solidification problem without latent heat effect is also considered in this study. The compared temperature distribution at $(x, y = 0)$ is presented in Fig. 12.

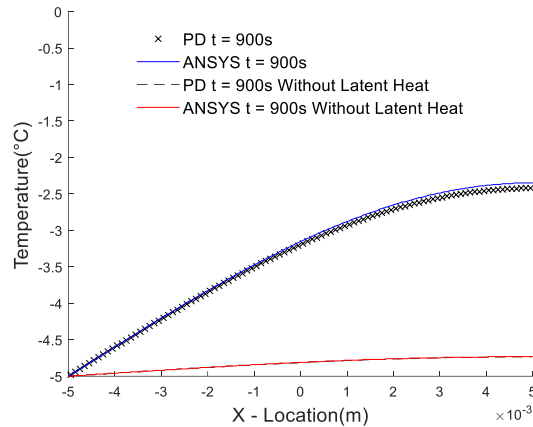


Fig. 12. Temperature distribution along $(x, y = 0)$ at $t=900s$.

As can be observed from the figure, the latent heat makes a substantial difference on the temperature distribution in phase change.

5.2 Neumann's solidification problem

Neumann [10] solved a more general phase change problem for which the substance does not initially stay at the fusion temperature. As shown in Fig. 13, the matter initially stays at a constant temperature θ_l , which is exceeding the fusion temperature θ_f . The side at one edge of the matter is rapidly maintained at temperature $\theta_b < \theta_l$. The solid-liquid boundary occurs immediately at the side and propagates through the liquid phase.

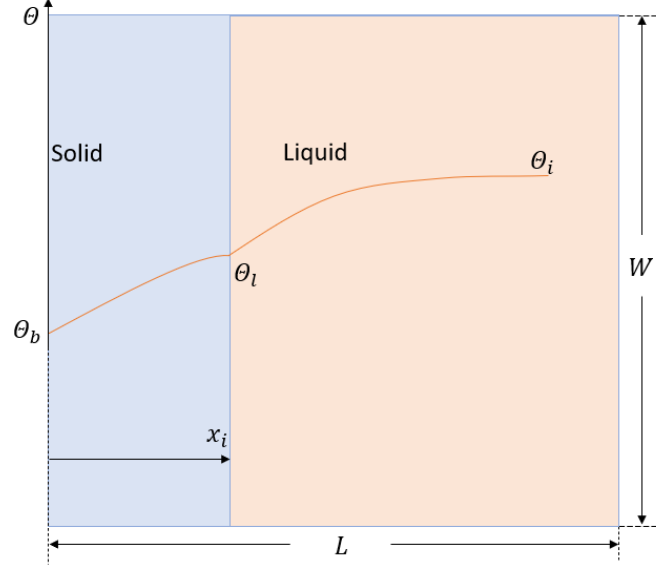


Fig. 13. Physical illustration of Neumann's solidification problem.

In the second case, a solidification phenomenon of a region is considered and constructed by the identical material with the first case. The geometry has length of $L = 0.01\text{m}$ and width of $W = 0.01\text{m}$ same as in Fig. 8(a).

The liquid field initially stays at a uniform temperature, $\theta_l = 2^\circ\text{C}$. Then, the left edge is suddenly subjected to a temperature of $\theta_b = -5^\circ\text{C}$ at $x = -\frac{L}{2}$ which is below the fusion temperature. The substance is assumed to undergo phase change in the phase transformation temperature range. Consequently, the border x_i between two phases begins solidifying at $x = -\frac{L}{2}$ starting from $t = 0\text{s}$. Its thermal conductivity and density are defined as $k=0.6\text{W/m}^\circ\text{C}$, and $\rho=1000\text{kg/m}^3$, respectively.

The latent heat required for the substance undergoing phase change is investigated. Hence, the specific heat at different phases is stated in Eq. (25). As shown in Fig. 8(b), the mesh between material points in peridynamic discretization is $\Delta x = L/100$. The horizon is selected as $\delta = 3\Delta x$. Time step size of $\Delta t = 3 \times 10^{-2}\text{s}$ is utilised.

The initial temperature is applied as

$$\theta(x, y, t = 0) = 2^\circ\text{C} \quad (28)$$

Fictitious boundary R_c with one horizon size is added to apply the temperature boundary condition, i.e.

$$\theta \left(x = -\frac{L}{2}, y, t \right) = \theta_b = -5^\circ\text{C} \quad (29)$$

The temperature distribution along $(x, y = 0)$ at several time intervals ($t = 300\text{s}, t = 600\text{s}, t = 900\text{s}$) have been examined in both PD and FEM models. As can be noticed from Fig. 14, the temperature distribution has a linear distribution between -5°C and -1°C , and curves undergo a smooth non-linear transformation between -1°C and 0°C as the latent heat is accounted for phase change at this temperature interval.

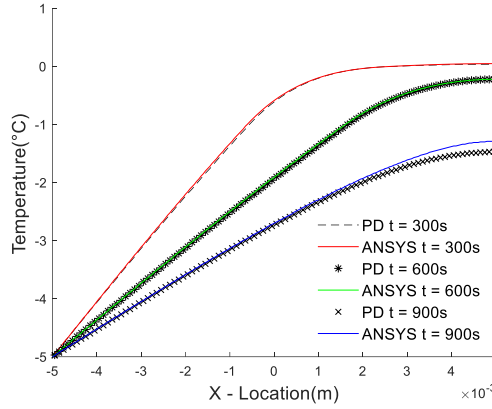


Fig. 14. Temperature comparison along $(x, y = 0)$ at several time intervals.

The temperature variations with time at two selected material points, $M \left(x = -\frac{4L}{5}, y = 0 \right)$ and $N \left(x = \frac{L}{2}, y = 0 \right)$ have been checked and compared with FEM. As can be observed from Fig. 15, the temperature undergoes a dramatic drop for material point M at the beginning compared with the temperature variation at material point N , as the interface starts solidifying at $x = -\frac{L}{2}$ from $t = 0\text{s}$ and point M is closer to the interface. Hence, the time for the moving interface passing point M is much shorter than the further end material point N .

The temperature at N has a quick drop between 2°C and 0°C while the curvature tends to smooth between 0°C and -1°C due to the latent heat effect between 0°C and -1°C . When the temperature is below -1°C , the substance completely solidifies. Hence, the temperature variation has the similar curvature with the temperature between 2°C and 0°C .

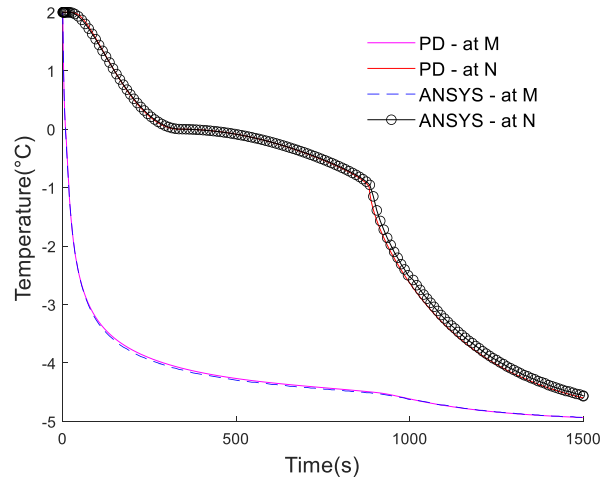


Fig. 15. Temperature variation at $M \left(x = -\frac{4L}{5}, y = 0 \right)$ and $N \left(x = \frac{L}{2}, y = 0 \right)$.

Fig. 16 compares the temperature distribution of the substance at 600s in both PD and FEM models. As can be seen from these figures, the PD model results match well with the FEM model results.

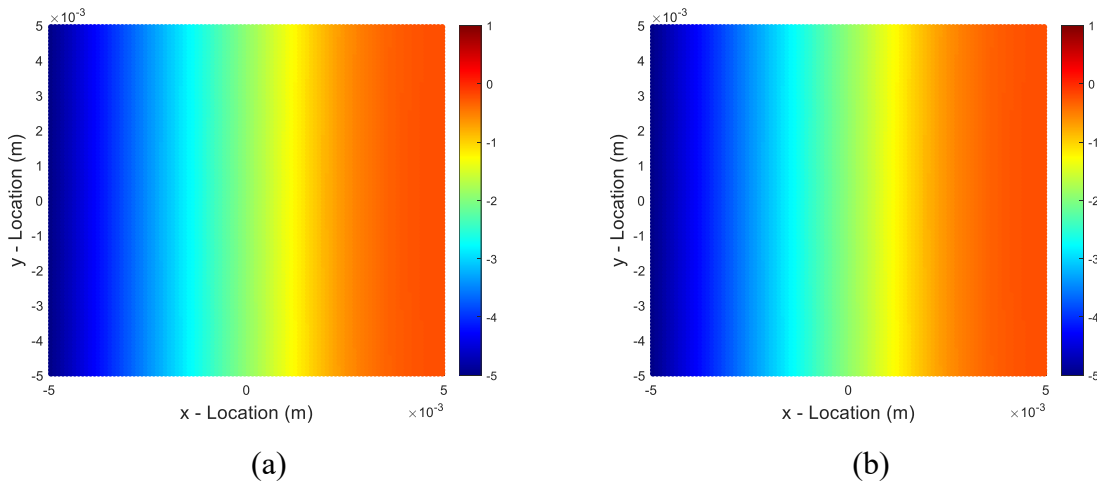


Fig. 16. Temperature distribution at $t=600s$ (a) PD (b) FEM model

5.3 Thermal analysis for a plate with a moving point heat source

An isotropic square plate with dimensions $L = W = 0.1$ m and thickness $H = 0.01$ m is presented in Fig. 17. The plate is subjected to a traveling point heat source $P = 3200W$, which is initially located at the centre of the plate and moves towards to the positive x coordinate direction with a velocity of $v = 0.005m/s$. The specific heat capacity, thermal conductivity and density are specified as $C_v=460$ J/kg, $k =50$ W/m°C, and $\rho=7820$ kg/m³, respectively.

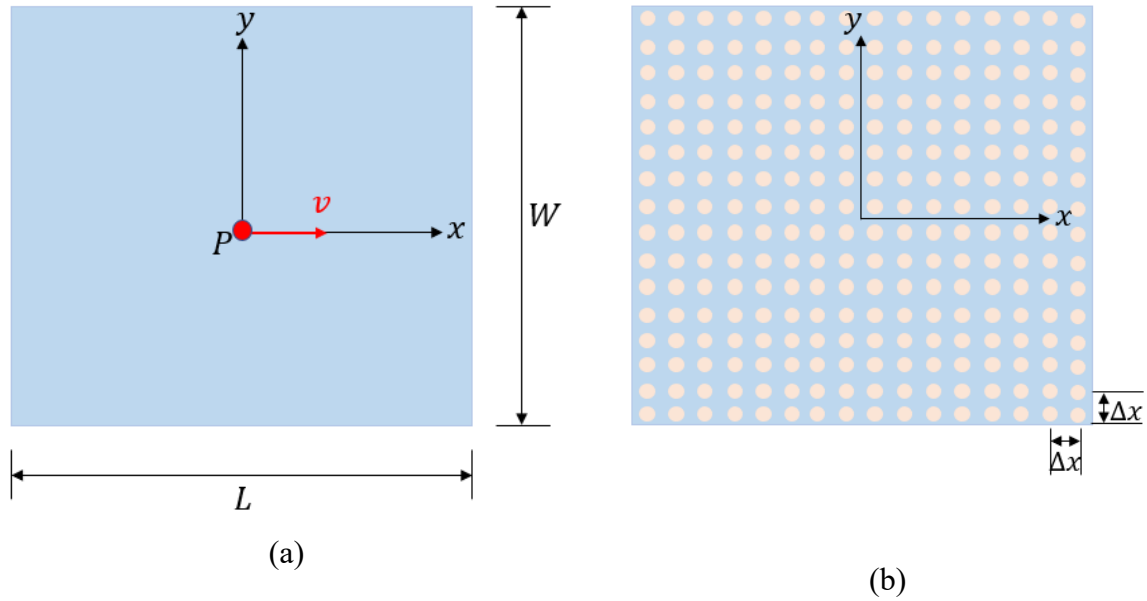


Fig. 17. Point heat source model illustration (a) geometry and (b) PD discretization.

As shown in Fig. 17(b), the material points are discretised with a uniform spacing $\Delta x = 0.0004\text{m}$ in x and y directions, respectively. The time step size is specified as $\Delta t = 5 \times 10^{-4}\text{s}$. The horizon is chosen as $\delta = 3\Delta x$.

In Finite Element model, the transient thermal conduction analysis does not incorporate a concentrated point heat source. To consider a concentrated point load heat source, the common approach is to apply point heat source employed as a volumetric heat generation and loaded on the selected elements.

In peridynamic modelling of point heat source, it follows a similar procedure with the Finite Element Method. The heat flow is implemented as a volumetric heat generation. Four material points shown around the point heat source in Fig. 18 have been selected to convert the point source into the volumetric heat generation on material points.

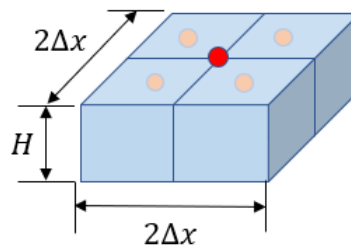


Fig. 18. Point heat source converted to heat generation.

The time-dependent point heat source is implemented by material points death-live procedure as stated in the section 4.1.3 while corresponding volumetric heat generation applied on material points is obtained as

$$h_q(x, t) = \frac{P}{4\Delta x^2 H} \quad (30)$$

The initial temperature of the plate is stated as

$$\theta_0(x, y, t = 0) = 0^\circ\text{C} \quad (31)$$

In order to validate the proposed peridynamic point heat source model in welding, the simulated temperature field along $(x, y = 0)$ is compared with the analytical solution [1] and FEM models at time=4s and shown in Fig. 19.

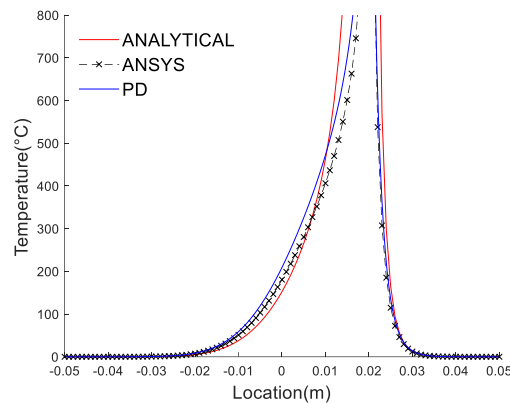


Fig. 19. Temperature variation along $(x, y = 0)$ at $t = 4s$.

As can be observed from the expression of analytical solution in Eq. (9), the temperature approaches to infinity at the centre of the point heat source. This is due to the limitation of the analytical model. PD model has a close agreement with analytical and finite element models for the material points located at the far region from the point heat source. A slight difference is observed with the analytical model.

The analytical model assumes that the point heat source can travel to a location at an instant time. However, on the numerical side, the point heat source is converted to a volumetric heat generation and applied on the element or material point in the Finite Element Model or peridynamic model, respectively. Hence, the predicted temperature field is robustly affected by the discretization in the numerical model. The numerical difference with the analytical

model can be minimized with an appropriate mesh size and a refined time step size; however, the computational time will increase correspondingly.

5.4 Thermal analysis for a block with a moving 3D ellipsoidal heat source

To demonstrate the capability of the proposed peridynamic formulation in welding heat conduction analysis, a three-dimensional ellipsoidal heat source model with $Q = 3200W$ acting on a rectangular metal block is investigated. As demonstrated in Fig. 20, the block has a dimension of $L = W = 0.1m$ with a thickness H of is $0.01m$. The ellipsoidal heat source is moving with a speed of $v=0.005m/s$ in positive x -direction from the centre of the block. The thermal conductivity and density are specified as $k = 50W/m^{\circ}C$ and $\rho=7820kg/m^3$, respectively.

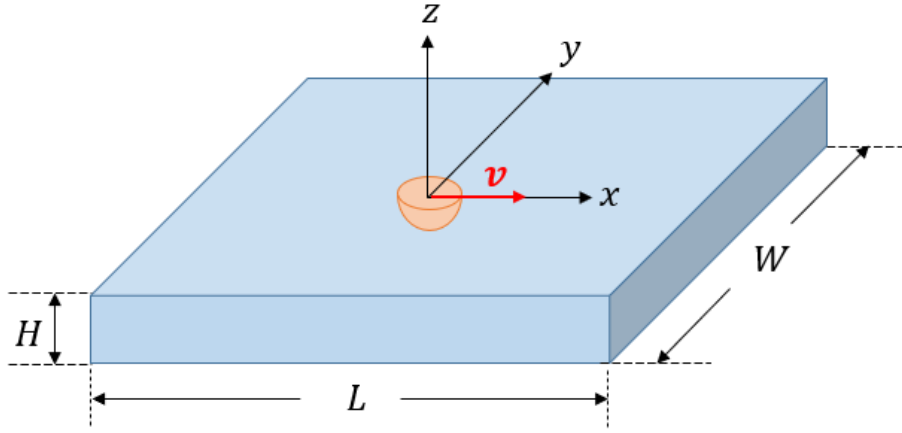


Fig. 20. Geometrical illustration of ellipsoidal heat source acting on a rectangular block.

The three-dimensional ellipsoidal heat source model subjected on the block can be expressed as

$$q(x, y, z, t) = q_m \exp\left(-\frac{3(x - v * t)^2}{c_h^2} - \frac{3y^2}{a_h^2} - \frac{3z^2}{b_h^2}\right) \quad (32)$$

and

$$q_m = \frac{6\sqrt{Q}}{a_h b_h c_h \pi \sqrt{\pi}} \quad (33)$$

where ellipsoidal heat source parameters a_h , b_h , and c_h are given as

$$a_h = 0.001m \quad (34a)$$

$$b_h = 0.001m \quad (34b)$$

$$c_h = 0.0005m \quad (34c)$$

The uniform spacing between material points in x, y and z directions in peridynamic discretization is $\Delta x = 4 \times 10^{-4}$. The horizon is chosen as $\delta = 3\Delta x$. Time step size of $\Delta t = 5 \times 10^{-4}$ s is used.

The initial temperature is set as

$$\theta(x, y, t = 0) = \theta_i = 0^\circ\text{C} \quad (35)$$

5.4.1 Ignoring Phase Change

In the first simulation for ellipsoidal heat source, the latent heat for substance to process phase change is not considered. Hence, the specific heat capacity is specified as $C_v=490\text{J/kg}$. A finite element model is also created to justify the outcomes of the PD model. The ANSYS element type Solid 70 is employed in the FEM with an element size of 0.001m in x and y -directions, and 0.0001m in the z -direction.

The compared temperature field at $t= 4\text{s}$ along heat source moving track at $(x, y = 0, z = \frac{H}{2})$ for both models are presented in Fig. 21. The developed peridynamic heat conduction model for ellipsoidal heat source is closely agreed with the FEM model.

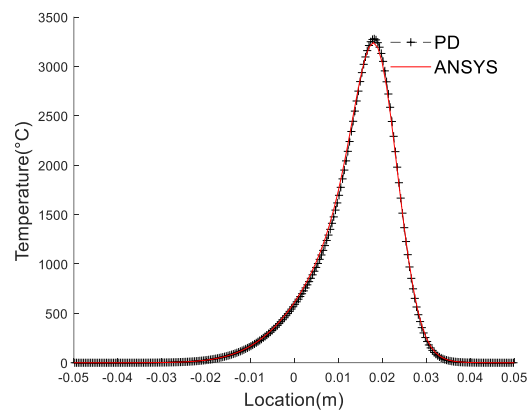


Fig. 21. Temperature variation at $(x, y = 0, z = \frac{H}{2})$ at $t = 4\text{s}$.

The predicted temperature fields of the block by using PD and FEM models are also presented in Fig. 22.

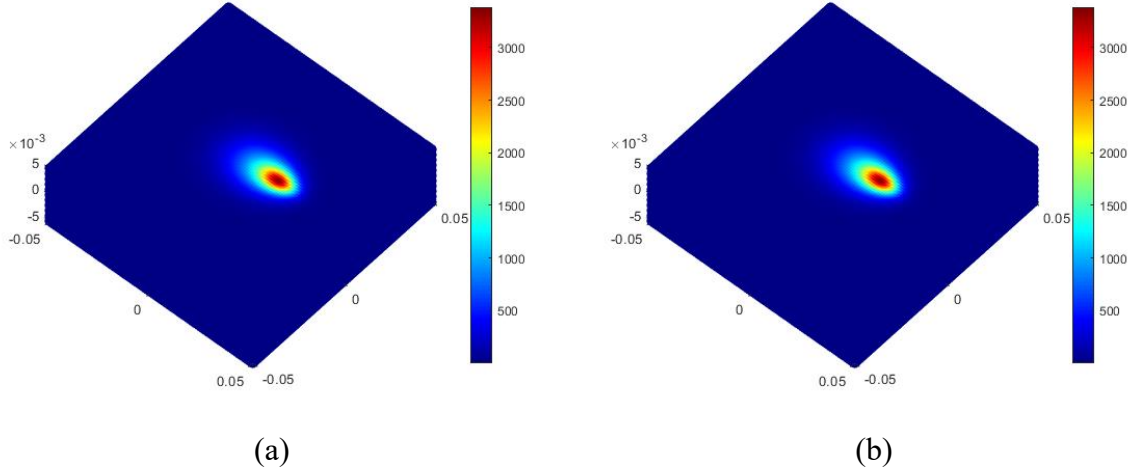


Fig. 22. Temperature distribution at $t=4s$ (a) PD (b) FEM model.

As can be noticed, the predicted temperature distribution on the block has a good agreement with the FEM model.

5.4.2 Considering Phase Change

In second investigation for ellipsoidal heat source model, phase change is considered. The mushy zone for metal is considered as $\theta_s = 1385^\circ\text{C} < \theta < \theta_l = 1450^\circ\text{C}$. The total latent heat required for the phase change completed is 260 kJ/kg .

Therefore, the effective heat capacity for metal at mushy zone is defined as.

$$C_p = \frac{L_T}{\theta_l - \theta_s} = 4000 \text{ J/kg}^\circ\text{C} \quad (36)$$

Thus, the effective specific heat capacity at different temperatures can be expressed as

$$C_v = \begin{cases} C_s = 490 \text{ J/kg}^\circ\text{C} & \theta < 1385^\circ\text{C} \\ C_p = 4000 \text{ J/kg}^\circ\text{C} & 1385^\circ\text{C} < \theta < 1450^\circ\text{C} \\ C_l = 490 \text{ J/kg}^\circ\text{C} & \theta > 1450^\circ\text{C} \end{cases} \quad (37)$$

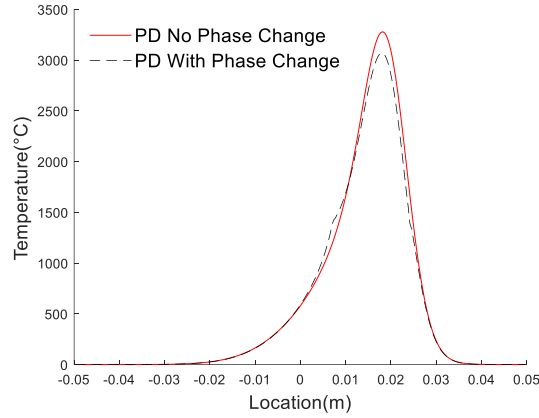


Fig. 23. Temperature variation along $(x, y = 0, z = \frac{H}{2})$ at $t=4s$.

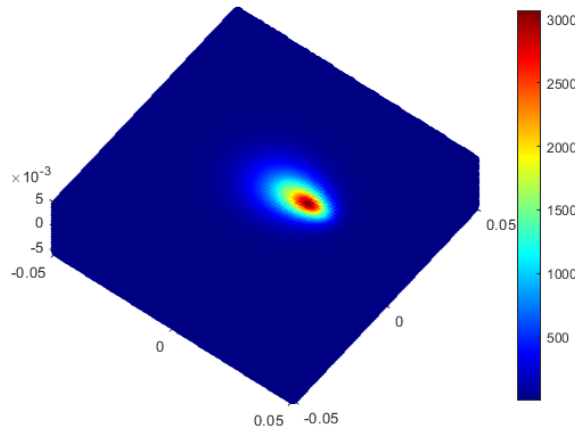


Fig. 24. Temperature distribution at $t=4s$ with phase change considered in PD model.

Fig. 23 compares the temperature distribution along $(x, y = 0, z = \frac{H}{2})$ when the phase change is considered in the heat conduction model. The metal block temperature field predicted by PD is presented in Fig. 24. As can be observed from the figures, when the phase change is considered in the model, the predicted temperature field shows a slow variation at the phase change temperature interval. The temperature is changed to steep variation again when the phase change has been completed. During the phase change, a large amount of energy is absorbed without significant temperature variation. As a result, the predicted maximum temperature in the phase change case is lower when compared with the case the phase change is neglected.

5.5 Thermomechanical analysis for a plate with moving 2D Gaussian heat source

The laser beam arc is frequently used in arc welding. The arc can be simplified by a heat source in the form of Gaussian distribution. Therefore, to present the capability of peridynamic model for thermomechanical phase change analysis in welding, a heat source model in the form of a Gaussian distribution acting on a two-dimensional plate has been investigated.

As shown in Fig. 25(a), plate has $L=0.1\text{m}$ in length, $W=0.1\text{m}$ in width, and a thickness of $H = 0.01\text{m}$. The Gaussian heat source with power $Q = 3200\text{W}$ is moving with a speed of $v=0.025\text{m/s}$ in positive x -direction from the centre of the plate. The thermal conductivity, density and thermal expansion coefficient are specified as $k = 50\text{W/m}^\circ\text{C}$, $\rho=7820\text{kg/m}^3$ and $\alpha = 13 \times 10^{-6} \text{ }^\circ\text{C}^{-1}$, respectively.

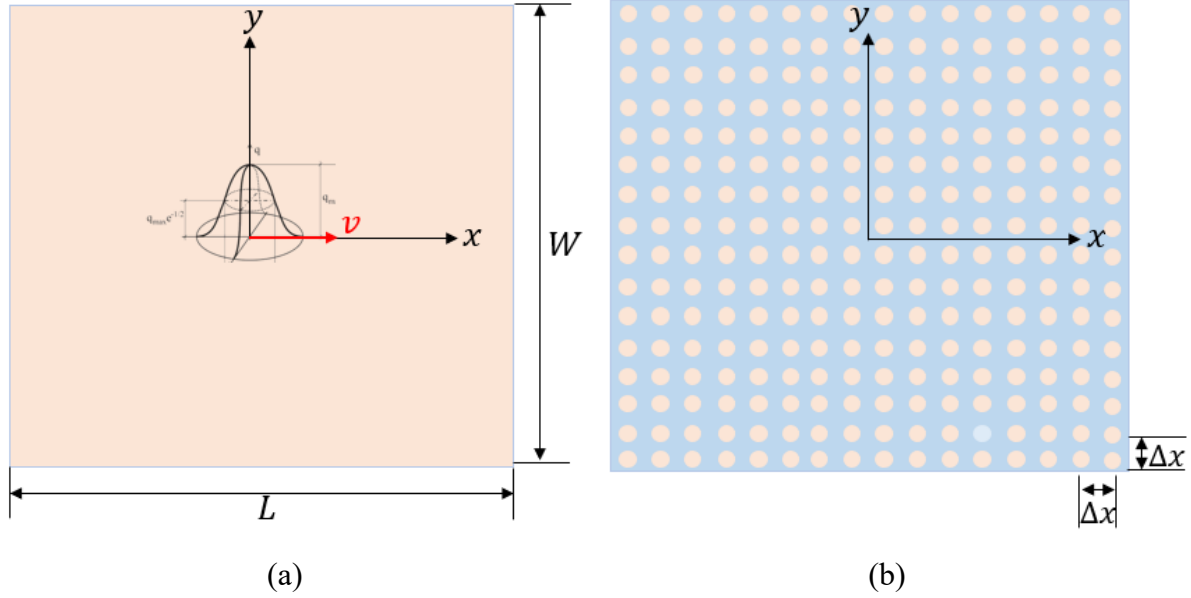


Fig. 25. Gaussian heat source model illustration (a) geometry and (b) PD discretization. Fig. 25(b) presents the peridynamic discretization model. The plate is meshed with a uniform spacing of $\Delta x = 4 \times 10^{-4}$ with a horizon size of $\delta = 3\Delta x$. The time step size is taken as $\Delta t = 1 \times 10^{-7}\text{s}$.

The Gaussian heat source acted on the plate has a form of

$$q(x, y, t) = \frac{Q}{2\pi\sigma^2} \exp\left(-\frac{(x - v * t)^2 + y^2}{2\sigma^2}\right) \quad (38)$$

where distribution parameter is selected as $\sigma = 0.0007\text{m}$. The proposed Gaussian distributed heat flux is converted to a volumetric heat generation per unit volume $h_q(x, y, t)$ in peridynamic heat conduction equation. This is achieved by

$$h_q(x, y, t) = \frac{q(x, y, t)}{\Delta x} \quad (39)$$

The initial temperature condition is specified as

$$\theta(x, y, t = 0) = \theta_i = 0^\circ\text{C} \quad (40)$$

5.5.1 Ignoring Phase Change

In the first case of thermomechanical analysis for Gaussian heat source model, the latent heat in the phase transformation is not implemented in the specific heat capacity. Then, a specific heat capacity of $C_v=490\text{J/kg}$ is applied. The Young's Modulus is specified as $E = 200\text{GPa}$.

To verify temperature and displacement fields in the PD model, a finite element model is also created. ANSYS element PLANE223 is used for thermomechanical analysis in FEM. The element size is specified as $\Delta = 0.001\text{m}$ in x and y -directions.

Fig. 26 and Fig. 27 compare the temperature field and displacement field at $t=0.08\text{s}$ along the heat source moving track ($x, y = 0$), respectively. In both models, close agreements are observed between ANSYS (FEM) and PD results.

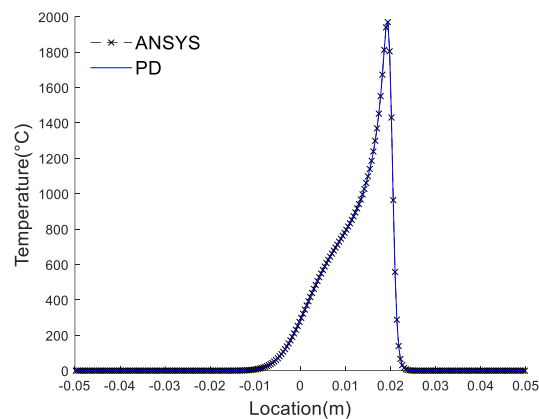


Fig. 26. Temperature variation along ($x, y = 0$) at $t=0.08\text{s}$.

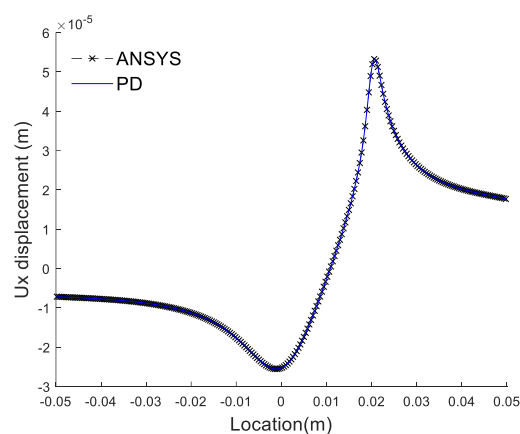


Fig. 27. Displacement variation along ($x, y = 0$) at $t=0.08\text{s}$.

Fig. 28 presents the temperature field of the plate in PD and FEM models. The FEM model results agree with the temperature field results predicted by the PD model.

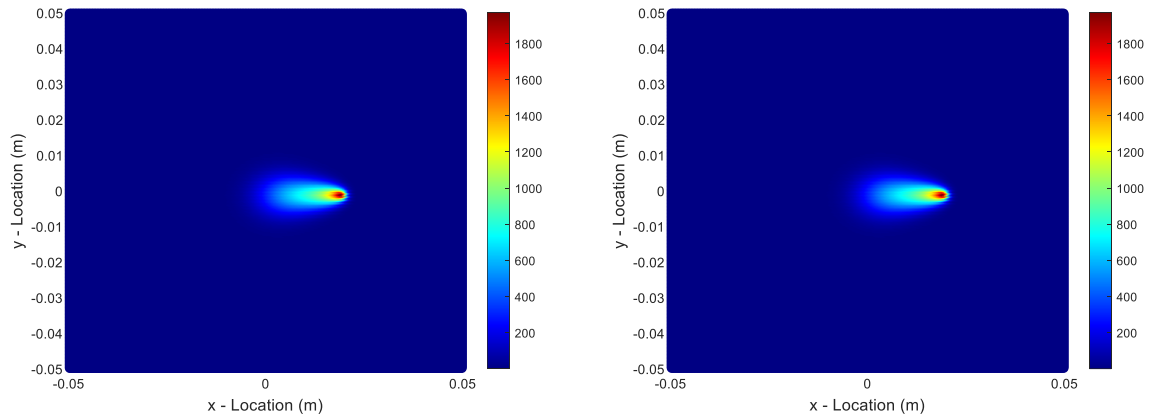


Fig. 28. Temperature field distribution at $t=0.08s$ (a) PD (b) FEM model.

5.5.2 Considering Phase Change

In the second case, phase change is considered. The latent heat in phase transformation is implicitly applied in effective heat capacity and same as stated in Eq. (37). The temperature-dependent Young's Modulus $E(\theta)$ is provided in Table 1.

Table 1. Temperature-dependent Young's Modulus

θ (K)	$E(\theta)$ (GPa)
298	200
473	187
673	172
873	157
973	141
1673	106
1573	10

The difference of the temperature distribution along heat source moving track ($x, y = 0$) when phase change is included is demonstrated in Fig. 29. The observation shows that when latent heat is concerned in the phase change, the predicted maximum temperature is lower than the case which does not consider the phase change.

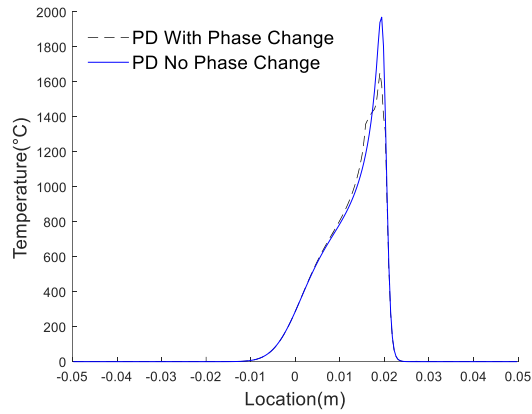


Fig. 29. Temperature variation along $(x, y = 0)$ at $t=0.08s$.

The horizontal displacement field along $(x, y = 0)$ is presented in Fig. 30. In addition, Fig. 31 (a) and (b) present the two-dimensional displacement fields when phase change is considered and omitted, respectively. It can be noticed that when the effect of temperature is taken into account for Young's Modulus, it has a significant effect on the displacement field.

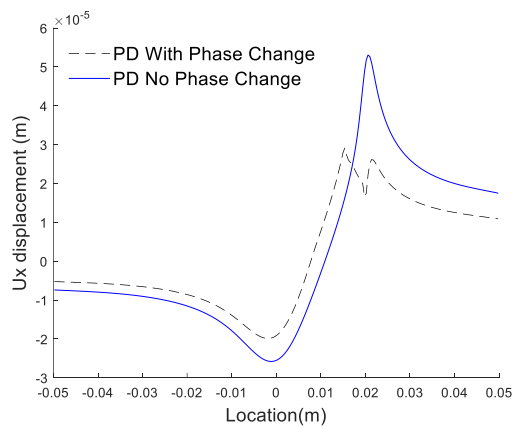


Fig. 30. Horizontal displacement variation along $(x, y = 0)$ at $t=0.08s$.

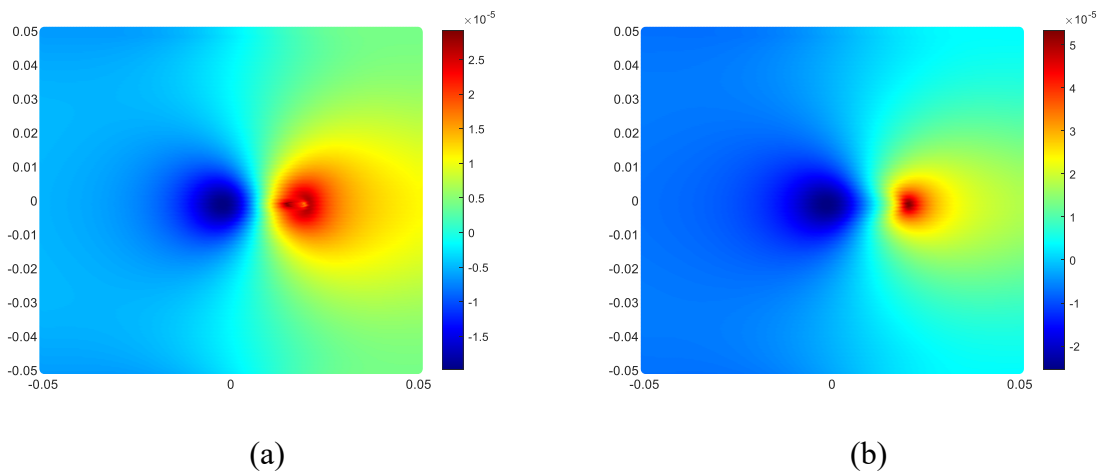


Fig. 31. Horizontal displacement field at $t=0.08s$ (a) With phase change (b) Without phase change.

6. Conclusions

In this study, a new non-linear transient peridynamic model has been proposed for thermomechanical analysis of welding process. Phase change, as a common physical process in heat transfer scenarios, is considered in the model. Several classical phase change problems, i.e. Stefan's and Neumann's solidification problems, are simulated by the proposed model. In addition, a wide range of commonly utilized time-dependent heat source models, i.e. Point, Gaussian, and volumetric distributed heat source model, which are related to the different welding methods in the manufacturing process, have been considered in the peridynamic heat transfer model and thermoelastic analysis. The predicted thermal and mechanical fields have been verified with the finite element model. The PD predicted results have a good agreement with the FEM model results. The phase change is a critical phenomenon in heat transfer. This is highlighted in the Gaussian and ellipsoidal heat source model. The effect of phase change on temperature and displacement fields are presented. Without considering the latent heat in the phase transformation can result in inaccurate temperature and displacement fields.

Reference

- [1] Rosenthal D. Mathematical theory of heat distribution during welding and cutting. *Weld J* 1941; 20:220-34.
- [2] Eagar TW, Tsai NS. Temperature fields produced by traveling distributed heat sources. *Weld J* 1983; 62(12):346-55.
- [3] Goldak J. A double ellipsoid finite element model for welding heat sources. *IIW Doc* 1985; 212.
- [4] Nguyen NT, Ohta A, Matsuoka K, Suzuki N, Maeda Y. Analytical solutions for transient temperature of semi-infinite body subjected to 3-D moving heat sources. *Weld J* 1999; 78:265-s.
- [5] Bian P, Shao X, Du J. Finite Element Analysis of thermal stress and thermal deformation in typical part during SLM. *Appl Sci* 2019; 9(11):p.2231.
- [6] Goldak J, Chakravarti A, Bibby M. A new finite element model for welding heat sources. *Metall Trans B* 1984;15(2):299-305.

- [7] Van Elsen M, Baelmans M, Mercelis P, Kruth JP. Solutions for modelling moving heat sources in a semi-infinite medium and applications to laser material processing. *Int J Heat Mass Transf* 2007; 50(23-24):4872-82.
- [8] Ning J, Sievers DE, Garmestani H, Liang SY. Analytical thermal modeling of metal additive manufacturing by heat sink solution. *Mater* 2019; 12(16):p.2568.
- [9] Biot MA. Thermoelasticity and irreversible thermodynamics. *J Appl Phys* 1956; 27(3): 240-53.
- [10] Jiji Latif M. Heat conduction. Berlin and Heidelberg: Springer-Verlag; 2009.
- [11] Hu H, Argyropoulos SA. Mathematical modelling of solidification and melting: a review. *Model Simul Mat Sci Eng* 1996; 4(4): p.371.
- [12] Yang H, He Y. Solving heat transfer problems with phase change via smoothed effective heat capacity and element-free Galerkin methods. *Int Commun Heat Mass Transf* 2010; 37(4):385-92.
- [13] Özişik MN. Heat conduction. New York: John Wiley & Sons;1993.
- [14] Madenci E, Oterkus E. Peridynamic Theory and Its Applications. New York: Springer; 2014.
- [15] Diyaroglu C, Oterkus S, Oterkus E, Madenci E, Han S, Hwang Y. Peridynamic wetness approach for moisture concentration analysis in electronic packages. *Microelectron Reliab* 2017; 70:103-11.
- [16] Kefal A, Sohoulis A, Oterkus E, Yildiz M, Suleman A. Topology optimization of cracked structures using peridynamics. *Contin Mech Thermodyn* 2019; 31(6): 1645-72.
- [17] Yang Z, Vazic B, Diyaroglu C, Oterkus E, Oterkus S. A Kirchhoff plate formulation in a state-based peridynamic framework. *Math Mech Solids* 2020; 25(3);727-38.
- [18] Vazic B, Wang H, Diyaroglu C, Oterkus S, Oterkus E. Dynamic propagation of a macrocrack interacting with parallel small cracks. *AIMS Mater Sci* 2017; 4(1):118-36.
- [19] Candaş A, Oterkus E, İmraç CE. Dynamic crack propagation and its interaction with micro-cracks in an impact problem. *J Eng Mater Technol* 2021; 143(1):011003.

- [20] Ozdemir M, Kefal A, Imachi M, Tanaka S, Oterkus E. Dynamic fracture analysis of functionally graded materials using ordinary state-based peridynamics. *Compos Struct* 2020; 244:p.112296.
- [21] Candaş, A., Oterkus, E. and İmrak, C.E., 2021. Peridynamic simulation of dynamic fracture in functionally graded materials subjected to impact load. *Eng Comput*, pp.1-15.
- [22] De Meo D, Russo L, Oterkus E. Modeling of the onset, propagation, and interaction of multiple cracks generated from corrosion pits by using peridynamics. *J Eng Mater Technol* 2017; 139(4):p.041001.
- [23] Huang Y, Oterkus S, Hou H, Oterkus E, Wei Z, Zhang S. Peridynamic model for visco-hyperelastic material deformation in different strain rates. *Contin Mech Thermodyn* 2019;1-35.
- [24] Kilic B, Madenci E. Peridynamic theory for thermomechanical analysis. *IEEE Trans Adv Packag* 2009; 33(1):97-105.
- [25] Oterkus S, Madenci E, Agwai A. Peridynamic thermal diffusion. *J Comput Phys* 2014; 265:71-96.
- [26] Alpay S, Madenci E. Crack growth prediction in fully-coupled thermal and deformation fields using peridynamic theory. In *54th AIAA/ASME/ASCE/AHS/ASC structures, structural dynamics, and materials conference 2013* (p. 1477).
- [27] D'Antuono P, Morandini M. Thermal shock response via weakly coupled peridynamic thermo-mechanics. *Int J Solids Struct* 2017; 129:74-89.
- [28] Hu Y, Chen H, Spencer BW, Madenci E. Thermomechanical peridynamic analysis with irregular non-uniform domain discretization. *Eng Fract Mech* 2018; 197:92-113.
- [29] Song Y, Liu R, Li S, Kang Z, Zhang F. Peridynamic modeling and simulation of coupled thermomechanical removal of ice from frozen structures. *Meccanica* 2019; 1-16.
- [30] Zhang H, Qiao P. An extended state-based peridynamic model for damage growth prediction of bimaterial structures under thermomechanical loading. *Eng Fract Mech* 2018; 189:81-97.
- [31] Shou Y, Zhou X. A coupled thermomechanical nonordinary state-based peridynamics for thermally induced cracking of rocks. *Fatigue Fract Eng Mater Struct* 2020; 43(2):371-86.

- [32] Martowicz A, Kantor S, Pieczonka Ł, Bryła J, Roemer J. Phase transformation in shape memory alloys: a numerical approach for thermomechanical modeling via peridynamics. *Meccanica* 2021; 56(4):841-54.
- [33] Pathrikar A, Tiwari SB, Arayil P, Roy D. Thermomechanics of damage in brittle solids: A peridynamics model. *Theor Appl Fract Mech* 2021; 112:p.102880.
- [34] Giannakeas IN, Papathanasiou TK, Bahai H. Simulation of thermal shock cracking in ceramics using bond-based peridynamics and FEM. *J Eur Ceram Soc* 2018; 38(8):3037-48.
- [35] Wang F, Ma YE, Guo Y, Huang W. Study on thermally induced crack propagation behavior of functionally graded materials using a modified peridynamic model. *Adv Mater Sci Eng* 2020.
- [36] Chen W, Gu X, Zhang Q, Xia X. A refined thermo-mechanical fully coupled peridynamics with application to concrete cracking. *Eng Fract Mech* 2021; 242:p.107463.
- [37] Silling SA, Askari E. A meshfree method based on the peridynamic model of solid mechanics. *Computers & Structures* 2005; 83(17-18): 1526-35.
- [38] Oterkus S, Madenci E, Agwai A. Fully coupled peridynamic thermomechanics. *J Mech Phys Solids* 2014; 64:1-23.
- [39] Christensen N. Distribution of temperatures in arc welding. *Brit Weld J* 1965; 12(2).
- [40] Madenci E, Oterkus S. Ordinary state-based peridynamics for plastic deformation according to von Mises yield criteria with isotropic hardening. *J Mech Phys Solids* 2016; 86:192-219.